

A consistent derivation of soil stiffness from elastic wave speeds

David M. Riley, Itai Einav, and François Guillard
*Particles and Grains Laboratory, School of Civil Engineering,
The University of Sydney, Sydney, New South Wales 2006, Australia*
(Dated: December 5, 2023)

Elastic wave speeds are fundamental in geomechanics and have historically been described by an analytic formula that assumes *linearly* elastic solid medium. Empirical relations stemming from this assumption were used to determine *nonlinearly* elastic stiffness relations that depend on pressure, density, and other state variables. Evidently, this approach introduces a mathematical and physical disconnect between the derivation of the analytical wave speed (and thus stiffness) and the empirically generated stiffness constants. In our study, we derive wave speeds for energy-conserving (hyperelastic) and non-energy-conserving (hypoelastic) constitutive models that have a general dependence on pressure and density. Under isotropic compression states, the analytical solutions for both models converge to previously documented empirical relations. Conversely, in the presence of shear, hyperelasticity predicts changes in the longitudinal and transverse wave speed ratio. This prediction arises from terms that ensure energy conservation in the hyperelastic model, without needing fabric to predict such an evolution, as was sometimes assumed in previous investigations. Such insights from hyperelasticity could explain the previously unaccounted-for evolution of longitudinal wave speeds in oedometric compression. Finally, the procedure used herein is general and could be extended to account for other relevant state variables of soils, such as grain-size, grain-shape, or saturation.

I. INTRODUCTION

Accurate determination of wave speeds and small-strain stiffness is crucial for a thorough geotechnical evaluation of soil sediments [1, 2] and the precise design of geotechnical structures [3]. In geomechanics, the wave speeds are conventionally assumed to be equivalent to the ones derived for linear elastic materials [4–7]. Based on this assumption, empirical relations are obtained for the nonlinear stiffness and are found to be dependent on pressure, density, and other state variables. However, assuming the wave speeds are defined for a linear elastic solid is generally an oversimplification for porous media and inconsistent with empirical relationships, necessitating the exploration of more general nonlinear elastic models. Here, wave speeds are derived for non-energy-conserving hypoelastic as well as energy-conserving hyperelastic models, assuming a general stiffness dependence on pressure and density while ensuring mathematical consistency.

Conventionally, in geotechnical engineering, wave speeds are assumed to be characterised by a homogeneous, isotropic, linearly elastic solid. The resulting longitudinal and transverse wave speeds are defined as:

$$V_p = \sqrt{\frac{M_w}{\rho}}, \quad (1)$$

$$V_s = \sqrt{\frac{G_w}{\rho}}, \quad (2)$$

where M_w and G_w are the constrained and shear moduli, respectively. After experimentally measuring the wave speeds, the stiffness moduli M_w and G_w are found to

depend on the effective pressure p and solid fraction ϕ in soils. Generally, these empirical relations adopt the form [4]:

$$M_w = AH(\phi) \left(\frac{p}{p_a} \right)^b, \quad (3)$$

$$G_w = BH(\phi) \left(\frac{p}{p_a} \right)^b, \quad (4)$$

where A and B are constants, $p_a = 1$ Pa is a reference stress, b is the stress exponent reflecting nonlinear pressure dependency, and $H(\phi)$ is a general function of solid fraction ϕ . Note that the void ratio $e = \frac{1-\phi}{\phi}$ is normally adopted in geotechnical engineering rather than the solid fraction ϕ , but we opt for a description in terms of solid fraction for convenience. Typically, $\frac{1}{3} \lesssim b \lesssim \frac{1}{2}$ for particles spanning from perfectly spherical to angular [8], as validated through effective medium representation [9–11]. Furthermore, more advanced relations have been proposed to include general stress states [5, 12–14] and other state variables such as grain-size distribution [6, 15, 16], particle shape [17, 18], or fabric [7, 19]. However, within the current paper, we do not explore these options as we seek to solely understand the effect of pressure and density dependence on the wave speed.

Although these empirical relations have successfully captured experimental phenomena, it is crucial to note that they were determined by first assuming a linearly elastic isotropic continuum. This introduces a discrepancy between the assumed elastic wave speeds, as given by eqs. (1) and (2) and the retrieved empirical equations eqs. (3) and (4). fig. 1 highlights this inconsistency, where soils are known to have state-dependent

stiffness, yet state-independent linear elasticity is assumed to derive the wave speeds. Despite existing models that incorporate pressure dependence in their constitutive laws [20–23], wave speeds are usually not derived with consideration for pressure dependence. However, hyperelastic pressure-dependent models assuming specific pressure dependencies have recovered empirical relations under isotropic compression states [24] and uniaxial compression states that showed shearing alters the evolution of the longitudinal to transverse wave speed ratio [25].

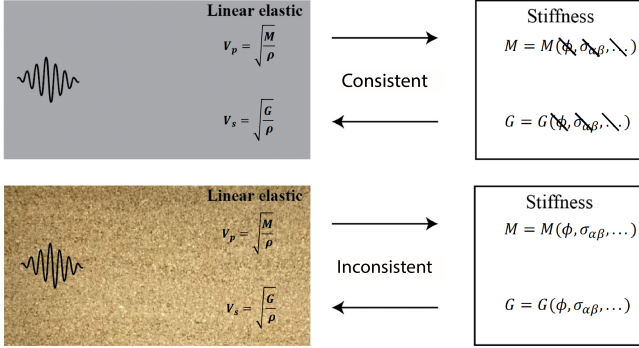


FIG. 1. Illustration of the inconsistency of assuming elastic wave speeds in soils. *Top row.* Linear elastic wave speeds are valid for materials in which stiffness is not a function of state. *Bottom row.* In soils, linear elastic wave speeds are assumed despite stiffnesses being a function of state. Here ϕ is solid fraction and $\sigma_{\alpha\beta}$ is the stress tensor.

Herein, analytical wave speeds are derived for both hyperelastic and hypoelastic constitutive models with a general pressure and density dependence. Importantly, the passage of energy is conserved in hyperelastic model, but this is not the case for the hypoelastic model. Furthermore, this derivation procedure remains accurate and general, irrespective of the model selected. The derived wave speeds reproduce the empirical relations under isotropic stress conditions regardless of whether hyperelasticity or hypoelasticity is considered. However, due to the density dependence, a minor, typically negligible, correctional term arises for the hyperelastic model. Conversely, when the material undergoes shear, the wave speed derived for hyperelasticity is significantly different than the hypoelastic wave speed because of the presence of additional non-negligible stress-dependent terms. These insights shed light on the evolution of the ratio between longitudinal and transverse wave speeds observed experimentally that previously could not be explained with empirical relations when assuming a linearly elastic isotropic continuum.

II. WAVE SPEED DERIVATION

We now derive the analytical expressions for longitudinal and transverse wave speeds. The momentum balance

is given by

$$\rho \ddot{u}_\alpha = \sigma_{\alpha\beta,\beta}, \quad (5)$$

where ρ is the bulk density, \ddot{u}_α represents acceleration in the α direction, $\sigma_{\alpha\beta}$ is the total stress tensor, and $\square_{,\alpha} = \frac{\partial \square}{\partial x_\alpha}$. For a homogeneously deformed solid at equilibrium, this simplifies to

$$\sigma_{\alpha\beta,\beta}^* = 0, \quad (6)$$

where $\sigma_{\alpha\beta}^*$ is the homogeneous reference (or unperturbed) stress. By first-order Taylor series expansion, the stress can be expressed in terms of $\sigma_{\alpha\beta}$ and a stress perturbation $\tilde{\sigma}_{\alpha\beta}$, and is given by

$$\sigma_{\alpha\beta} = \sigma_{\alpha\beta}^* + \tilde{\sigma}_{\alpha\beta} = \sigma_{\alpha\beta}^* + C_{\alpha\beta\gamma\zeta}^* \tilde{u}_{\gamma,\zeta} \quad (7)$$

where $C_{\alpha\beta\gamma\zeta}^*$ is the isotropic homogeneous elastic stiffness tensor at the reference state, \tilde{u}_α is a displacement perturbation from the reference homogeneous solution of the displacement field u_α^* , such that $u_\alpha = u_\alpha^* + \tilde{u}_\alpha$ [26, 27]. The strain tensor is defined as $u_{\gamma,\zeta} = \varepsilon_{\gamma\zeta}$, and thus, $\tilde{u}_{\gamma,\zeta} = \tilde{\varepsilon}_{\gamma\zeta}$ is the perturbed strain tensor. By inserting eq. (7) into eq. (6) and using a first-order Taylor expansion of the left-hand side, assuming no acceleration in the reference state ($\ddot{u}_\alpha^* = 0$) the momentum balance is expressed as

$$\rho^* \tilde{u}_\alpha = \tilde{\sigma}_{\alpha\beta,\beta} \quad (8)$$

where ρ^* is the homogeneous equilibrium density. The perturbed stress tensor $\tilde{\sigma}_{\alpha\beta}$ will be later determined from the constitutive law through first-order Taylor series expansion.

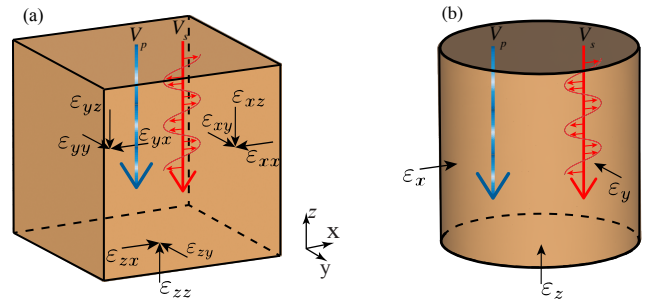


FIG. 2. Illustration of longitudinal wave (blue gradient line) and transverse wave (red) for (a) general case and (b) in triaxial conditions. For the longitudinal wave, the periodic gradient denotes material displaced in the z -direction, and the transverse wave has the material displaced in the x -direction, denoted by small red arrows. Both waves propagate in the z -direction.

First, consider longitudinal waves that propagate along the z -axis. The perturbed displacement \tilde{u}_z is decomposed in Fourier modes of the form $\tilde{u}_z = U_z e^{i(kz - \omega t)}$, where i is the unit imaginary number, k is the wave number, and

ω is the circular frequency. The perturbed strain tensor and its deviatoric component are thus expressed as

$$\tilde{\varepsilon}_{\alpha\beta} = ik\tilde{u}_z \begin{bmatrix} 0 & 0 & 0 \\ 0 & 0 & 0 \\ 0 & 0 & 1 \end{bmatrix}, \quad \tilde{\varepsilon}'_{\alpha\beta} = ik\tilde{u}_z \begin{bmatrix} -\frac{1}{3} & 0 & 0 \\ 0 & -\frac{1}{3} & 0 \\ 0 & 0 & \frac{2}{3} \end{bmatrix}, \quad (9)$$

where $\tilde{\varepsilon}'_{\alpha\beta} = \tilde{\varepsilon}_{\alpha\beta} - \frac{1}{3}\tilde{\varepsilon}_{\gamma\gamma}\delta_{\alpha\beta}$ is the deviatoric component of the perturbed strain tensor with $\delta_{\alpha\beta}$ being the Kronecker delta.

For a transverse wave, we assume that the wave propagates in the z-axis and is polarised in the x-direction, where the perturbed displacement $\tilde{u}_x = U_x e^{i(kz - \omega t)}$. The disturbance to the strain field and its deviatoric component for the transverse wave are equal in this case and given by

$$\tilde{\varepsilon}_{\alpha\beta} = \tilde{\varepsilon}'_{\alpha\beta} = ik\tilde{u}_x \begin{bmatrix} 0 & 0 & \frac{1}{2} \\ 0 & 0 & 0 \\ \frac{1}{2} & 0 & 0 \end{bmatrix}. \quad (10)$$

fig. 2 (a) illustrates these wave perturbations for a general state, where the periodic blue arrow shows the longitudinal wave and the red displays the transverse wave. The periodic gradient shows that the particle motion is in the same direction as the wave propagation for the longitudinal wave. In contrast, the particle motion occurs perpendicular to the wave direction in the transverse wave case.

To determine the wave speed, a constitutive model is required to define the isotropic homogeneous elastic stiffness tensor, as this enables an explicit representation of eq. (8) following the substitution of the perturbed strains into the perturbed stress. The following section describes two potential constitutive relations to apply these strain perturbations.

A. Hyperelastic wave speed

Now that a general framework for wave speed derivations has been laid, a constitutive law is required to evaluate the perturbed stress. We begin by introducing a hyperelastic model for pressure and density-dependent media. The advantage of hyperelasticity is that it ensures the energy is being conserved as waves travel through the medium, thus keeping faithful to the meaning of a true elastic body. Here, we consider an internal energy density \mathcal{U} that broadens previous work by [28], and depends on solid fraction ϕ and elastic strain tensor $\varepsilon_{\alpha\beta}$:

$$\mathcal{U} = F(\phi) \left(\frac{\bar{K}}{(1+n)(2+n)} \varepsilon_v^{n+2} + \bar{G} \varepsilon_v^n \varepsilon'_{\alpha\beta} \varepsilon'_{\alpha\beta} \right) \quad (11)$$

where \bar{K} is the bulk stiffness constant, \bar{G} is the shear stiffness constants, respectively; and $\varepsilon_v = \varepsilon_{\alpha\alpha}$ is the volumetric elastic strain. The choice of this energy form will be justified later. The pressure and deviatoric stress

are given through differentiation of the internal energy density

$$p = \frac{\partial \mathcal{U}}{\partial \varepsilon_v} = F(\phi) \left(\frac{\bar{K}}{n+1} \varepsilon_v^{n+1} + \frac{3}{2} n \bar{G} \varepsilon_v^{n-1} \varepsilon_s^2 \right), \quad (12)$$

$$\sigma'_{\alpha\beta} = \frac{\partial \mathcal{U}}{\partial \varepsilon'_{\alpha\beta}} = 2F(\phi) \bar{G} \varepsilon_v^n \varepsilon'_{\alpha\beta}, \quad (13)$$

where, $\sigma_{\alpha\beta} = \sigma'_{\alpha\beta} + p\delta_{\alpha\beta}$ is the total stress tensor, and $\varepsilon_s = \sqrt{\frac{2}{3} \varepsilon'_{\alpha\beta} \varepsilon'_{\alpha\beta}}$ is the triaxial shear strain invariant. It is worth noting the generality of the model above. Typically, we will choose $F(\phi) = \phi^{\bar{d}}$, with \bar{d} as a constant, where this form was motivated by experiments [29]. For example, linear elasticity is retrieved for $n = 0$ and $F(\phi) = 1$ ($\bar{d} = 0$). Furthermore, if $F(\phi) = \phi^{\bar{d}} \simeq \left(\frac{\rho}{\rho_s^*} \right)^{\bar{d}}$ is assumed, where ρ_s^* is the unstressed solid density, then depending on the choice of n and \bar{d} the model can recover a variety nonlinear elastic models, such as the ones described by Alaei *et al.* [28], Riley *et al.* [30], Chen *et al.* [31]. This versatile structure permits a comprehensive formulation that spans from linear elasticity to pressure-dependent nonlinear elastic material, aptly capturing the behaviour typically observed in experiments.

The perturbed stress of eqs. (12) and (13) can be determined by first-order Taylor series expansion about the homogeneous unperturbed (reference) strain, which gives

$$\begin{aligned} \tilde{p} &= F(\phi) \left[\left(\bar{K} \varepsilon_v^n + \frac{3}{2} n(n-1) \bar{G} \varepsilon_v^{n-2} \varepsilon_s^2 \right) \tilde{\varepsilon}_v + 3n \bar{G} \varepsilon_v^{n-1} \varepsilon_s \tilde{\varepsilon}_s \right] \\ &+ \frac{p}{F(\phi)} \frac{\partial F(\phi)}{\partial \phi} \phi \tilde{\varepsilon}_v, \end{aligned} \quad (14)$$

$$\begin{aligned} \tilde{\sigma}'_{\alpha\beta} &= F(\phi) (2n \bar{G} \varepsilon_v^{n-1} \varepsilon'_{\alpha\beta} \tilde{\varepsilon}_v + 2 \bar{G} \varepsilon_v^n \tilde{\varepsilon}'_{\alpha\beta}) \\ &+ \frac{\sigma'_{\alpha\beta}}{F(\phi)} \frac{\partial F(\phi)}{\partial \phi} \phi \tilde{\varepsilon}_v, \end{aligned} \quad (15)$$

where \square^* has been dropped from the homogeneous (reference) terms for brevity and the mass balance definition $\tilde{\phi} = \phi \tilde{\varepsilon}_v$ was used, assuming no solid density change, as expected in elastic wave experiments.

Consequently, by substituting perturbed strains eq. (9) and the perturbed stress eqs. (14) and (15) into eq. (8), and using the definition $\tilde{\varepsilon}_s = \frac{2}{3} \frac{\varepsilon'_x \varepsilon'_y \varepsilon'_z}{\varepsilon_s}$, the momentum balance for the hyperelastic model with a plane wave perturbation propagating along z can be written as

$$\begin{aligned} -\rho \omega^2 &= -k^2 F(\phi) \left(\bar{M} \varepsilon_v^n + \frac{3}{2} n(n-1) \bar{G} \varepsilon_v^{n-2} \varepsilon_s^2 \right. \\ &\left. + 2n \bar{G} \varepsilon_v^{n-1} \varepsilon'_{zz} + 2n \bar{G} \varepsilon_v^{n-1} \sum_{\beta=x}^z \varepsilon'_{z\beta} \right) - k^2 \frac{\phi \sigma_{zz}}{F(\phi)} \frac{\partial F(\phi)}{\partial \phi}, \end{aligned} \quad (16)$$

where $\bar{M} = \bar{K} + \frac{4}{3}\bar{G}$ is the constrained modulus, and all state variables are defined in terms of homogeneous unperturbed states. Notably, this result showcases that while the perturbation is along the z -axis, there emerges a dependence on the unperturbed states in the state of other directions, *i.e.*, $\varepsilon'_{z\beta}$. The wave speed of longitudinal waves is defined as $V_p = \frac{\omega}{k}$ [32, 33], which gives

$$\rho (V_p^{hyper})^2 = F(\phi) \left(\bar{M}\varepsilon_v^n + \frac{3}{2}n(n-1)\bar{G}\varepsilon_v^{n-2}\varepsilon_s^2 + 2n\bar{G}\varepsilon_v^{n-1}(\varepsilon'_{zx} + \varepsilon'_{zy} + 2\varepsilon'_{zz}) \right) + \frac{\phi\sigma_{zz}}{F(\phi)} \frac{\partial F(\phi)}{\partial \phi}. \quad (17)$$

Similarly, by substitution of eq. (10) and the perturbed stress eqs. (14) and (15) into eq. (8), the transverse wave speed of a wave propagating along z -direction and polarised along x -direction can be found to be

$$\rho (V_s^{hyper})^2 = F(\phi)\bar{G}\varepsilon_v^{n-1}(n\varepsilon'_{zx} + \varepsilon_v). \quad (18)$$

Notably, the longitudinal wave speed in eq. (17) and transverse wave speed in eq. (18) both depend on strain (or stress states) that cannot be represented solely by invariants, which are a result of the chosen wave perturbation direction and model. Thus, if different propagation or polarisation directions other than the ones illustrated in fig. 2 were used on the same unperturbed state, the wave speed would naturally depend on different strain components. However, as shown later, only the longitudinal wave speed maintains this dependence on directionality for triaxial conditions.

B. Tangent moduli for hyperelastic model

The particular choice of the internal energy density eq. (11) is motivated here. To this end, we will show that the tangent (instantaneous) moduli for the simplified scenario of zero shear strain is equivalent to eqs. (3) and (4). To begin, the constrained tangent modulus is determined by $M_t = C_{zzzz} = \frac{\partial \sigma_{zz}}{\partial \varepsilon_{zz}}$, which is found to depend on the volumetric strain and solid fraction as follows:

$$M_t = F(\phi) \left(\bar{M}\varepsilon_v^n + \frac{3}{2}n(n-1)\bar{G}\varepsilon_v^{n-2}\varepsilon_s^2 + 4n\bar{G}\varepsilon_v^{n-1}\varepsilon'_{zz} \right) + \left(\frac{\phi}{F(\phi)} \frac{\partial F(\phi)}{\partial \phi} \right) \sigma_{zz}. \quad (19)$$

Importantly, the right-hand side of the longitudinal wave speed in eq. (17) is equivalent to this modulus in the absence of deviatoric shear components $\varepsilon'_{xz} = \varepsilon'_{yz} = 0$.

In the absence of shear strain, which happens under isotropic stress states whereby the shear stresses are zero, it is readily shown by substituting eq. (12) that the con-

strained modulus simplifies to

$$M_t = F(\phi)\bar{M}\varepsilon_v^{\frac{b}{1-b}} + \left(\frac{\phi}{F(\phi)} \frac{\partial F(\phi)}{\partial \phi} \right) p, \quad (20a)$$

$$b = \frac{n}{1+n}, \quad (20b)$$

where we note an additional linear dependence on pressure, a structure that seems to differ greatly from observed empirical trends.

However, by recognising that $p \propto F(\phi)\bar{M}\varepsilon_v^{\frac{1}{1-b}}$, it is apparent that $F(\phi)\bar{M}\varepsilon_v^{\frac{b}{1-b}} \propto \frac{p}{\varepsilon_v}$. Furthermore, considering the reasonable and general choice [29] of $F(\phi) = \phi^{\bar{d}}$ the second term reduces to $\bar{d}p$. It is now clear that when assuming small elastic volumetric deformations $\varepsilon_v \ll 1$ that

$$F(\phi)\bar{M}\varepsilon_v^{\frac{b}{1-b}} \gg \left(\frac{\phi}{F(\phi)} \frac{\partial F(\phi)}{\partial \phi} \right) p. \quad (21)$$

Therefore, the approximate constrained tangent modulus can be expressed through substitution of eq. (12)

$$M_t = \frac{\partial \sigma_{zz}}{\partial \varepsilon_{zz}} \approx AH(\phi) \left(\frac{p}{p_a} \right)^b, \quad (22a)$$

$$A = \bar{M} \left(\frac{p_a}{(1-b)\bar{K}} \right)^b, \quad (22b)$$

$$H(\phi) = F(\phi)^{1-b}, \quad (22c)$$

where p_a was introduced such that A has units of stress. Similarly, the shear tangent modulus G_t with respect to triaxial shear strain with substitution of eq. (12) is

$$G_t = \frac{1}{3} \frac{\partial q}{\partial \varepsilon_s} = BH(\phi) \left(\frac{p}{p_a} \right)^b, \quad (23a)$$

$$B = \bar{G} \left(\frac{p_a}{(1-b)\bar{K}} \right)^b, \quad (23b)$$

where again p_a was introduced such that B has units of stress. Thus, under the assumption of isotropic conditions and small elastic strains ($\varepsilon_s = 0$, $\varepsilon_v \ll 1$), the tangent moduli reduce to the experimental forms found previously eqs. (3) and (4) in the hyperelastic model.

C. Hypoelastic wave speed

Hypoelastic models tend to adopt the experimentally developed empirical stiffness in eqs. (3) and (4) without the requirement of being determined from internal energy. Thus, hypoelastic models exhibit path-dependency and do not conform to the thermodynamic requirements of energy conservation [21, 34]. The stress rates determined directly from the empirical relations (eqs. (3) and (4)) are

$$\dot{p} = \bar{K}^{hyper} H(\phi) \left(\frac{p}{p_a} \right)^b \dot{\varepsilon}_v, \quad (24)$$

$$\dot{\sigma}'_{\alpha\beta} = 2\bar{G}^{hypo} H(\phi) \left(\frac{p}{p_a}\right)^b \dot{\varepsilon}'_{\alpha\beta}, \quad (25)$$

where \bar{K}^{hypo} and \bar{G}^{hypo} are the bulk and shear stiffness constants for the hypoelastic model, which have a stress dimension. The superscript emphasises that although these are elastic constants, their values is not inherently equal to those of the hyperelastic model.

Following a procedure similar to the derivation of the hyperelastic wave speeds, the perturbed stress is substituted into eq. (8). However, hypoelasticity does not have an explicit expression for total stress $\sigma_{\alpha\beta}$ and as such, it assumed that $\tilde{\sigma}_{\alpha\beta} = \dot{\sigma}_{\alpha\beta}$ as this was the result of the first-order Taylor expansion of eqs. (12) and (13). The resulting longitudinal and transverse wave velocities are

$$V_p^{hypo} = \sqrt{\frac{AH(\phi)}{\rho} \left(\frac{p}{p_a}\right)^b}, \quad (26a)$$

$$A = \left(\bar{K}^{hypo} + \frac{4}{3}\bar{G}^{hypo}\right), \quad (26b)$$

$$V_s^{hypo} = \sqrt{\frac{BH(\phi)}{\rho} \left(\frac{p}{p_a}\right)^b}, \quad (27a)$$

$$B = \bar{G}^{hypo}, \quad (27b)$$

which are equivalent to eqs. (1) and (2) when eqs. (3) and (4) are substituted, and thus, the empirical relations are recovered. However, the hypoelastic wave speeds lack the additional stress-dependent terms that emerged in the hyperelastic derivation due to the energy conservation of the latter model. These differences are critical to the comparison against experimental results that will be shown between the hyperelastic and the hypoelastic model in triaxial compression. Notably, A and B in eqs. (26b) and (27b) depend on the elastic constants differently than their counterparts in eqs. (22b) and (23b).

D. Linear elastic limit

For both the hyperelastic and hypoelastic models, linear elasticity is recovered when $b = 0$ and $H(\phi) = 1$. In this limit, the longitudinal wave speed and transverse wave speed for both hyperelastic and hypoelastic models reduce to

$$V_p = \sqrt{\frac{\bar{M}}{\rho}}, \quad (28)$$

$$V_s = \sqrt{\frac{\bar{G}}{\rho}}, \quad (29)$$

where the superscript notation is dropped as the stiffness constants for the hyperelastic and hypoelastic models are equivalent in this case. Therefore, eqs. (1) and (2) are recovered in the linear elastic limit.

TABLE I. Summary of effective model constants obtained for fitting with the isotropic experimental measurements. Note that $d = (1 - b)\bar{d}$ for the hyperelastic model.

A (MPa)	B (MPa)	b	d
95.27	31.40	0.35	5.32

TABLE II. Summary of model stiffness constants obtained for fitting with the isotropic experimental measurements. The stiffness constants \bar{K} and \bar{G} are determined from eqs. (22b) and (23b), while the stiffness constants \bar{K}^{hypo} and \bar{G}^{hypo} are determined from eqs. (26b) and (27b).

\bar{K} (MPa)	\bar{G} (MPa)	\bar{K}^{hypo} (MPa)	\bar{G}^{hypo} (MPa)
$62.1 \cdot 10^4$	$36.5 \cdot 10^4$	40.04	31.40

III. COMPARISON WITH EXPERIMENTAL RESULTS

A. Isotropic compression

In the isotropic compression scenario (*i.e.*, $\varepsilon_s = \varepsilon'_{\alpha\beta} = 0$), we show that the hyperelastic wave speeds eqs. (17) and (18) reduce to the same form as the wave speeds of the hypoelastic model eqs. (26a) and (27a). If eq. (12) while $\varepsilon_s = 0$ (isotropic compression) is substituted into eq. (17), then the longitudinal wave speed is

$$V_p^{hyper} \approx \sqrt{\frac{AH(\phi)}{\rho} \left(\frac{p}{p_a}\right)^b}. \quad (30)$$

where A is defined in eq. (22b) and the density correction term, *i.e.*, $\frac{\phi p}{F(\phi)} \frac{\partial F(\phi)}{\partial \phi}$, is ignored as discussed previously (cf. Eq. 21). Similarly, by substitution of eq. (12) into eq. (18), the corresponding transverse wave speed for the hyperelastic model is

$$V_s^{hyper} = \sqrt{\frac{BH(\phi)}{\rho} \left(\frac{p}{p_a}\right)^b}, \quad (31)$$

where B is defined in eq. (23b). The derived wave speeds are equivalent to the hypoelastic model (eqs. (26a) and (27a)). However, it is crucial to note that A and B are combined parameters of the bulk and shear stiffness constants, \bar{K} and \bar{G} , respectively. Therefore, to accurately determine the stiffness constants, both V_p and V_s must be measured for the hyperelastic and hypoelastic models.

Both models are fit to an experimental dataset of wave velocities to elucidate better the equivalence of these derived wave speeds and the empirical relations eqs. (3) and (4). The data was acquired by digitising results presented in [35]. The wave measurement was performed on Toyoura sand with a specific gravity of $G_s = 2.64$, a minimum void ratio of $e_{min} = 0.569$, and a maximum void ratio of $e_{max} = 0.936$. Notably, V_p and V_s were fit to experimental measurements simultaneously. Despite the

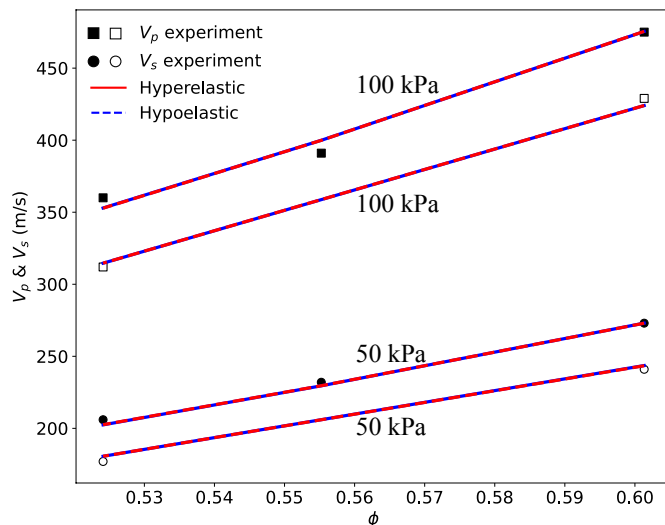


FIG. 3. Transverse wave velocity V_s and longitudinal wave velocity V_p against solid fraction ϕ for an isotropic stress state of 50 and 100 kPa. The empirical relations are not shown because they are proven to be equivalent to the wave speeds derived from the hypoelastic model. The experimental data was extracted from [35].

sparsity of data, both models fit the experimental results well, and their equivalency in this scenario is clear. The resulting coefficients are shown in table I, which will also be used for the following section. The stiffness constants for the hyperelastic and the hypoelastic model are shown in table II. Notably, the models have several order of magnitude differences between the elastic coefficients, but it is important to recall that these are from two different models, and therefore cannot be directly compared together. Moreover, the rather large elastic stiffness values of the hyperelastic model occur because once eqs. (22b) and (23b) are substituted into eqs. (30) and (31) it becomes clear that the pressure is scaled by \bar{K} as opposed to p_a as in the hypoelastic model.

B. Triaxial compression

While the wave speeds of both models are shown to be mathematically equivalent for isotropic compression, this is not the case for triaxial states. For the hypoelastic model, wave speeds do not change from eqs. (26a) and (27a) because they solely depend on ϕ and p . However, the hyperelastic model shows that stress dependence is more involved in triaxial states due to being derived from an energy potential. fig. 3 (b) shows the wave perturbations and relevant directions of propagation and particle motion along principle directions in this scenario. For the hyperelastic model, the longitudinal wave speed in triaxial conditions is equivalent to eq. (17), but since the reference state is in triaxial conditions, $\varepsilon'_{zx} = \varepsilon'_{zy} = 0$ and only $\varepsilon'_{zz} \neq 0$, while the transverse

wave speed eq. (18), by substitution of eq. (12), becomes

$$V_s^{hyper} = \sqrt{\frac{\bar{G}H(\phi)}{\rho} \left(\frac{p}{2(1-b)\bar{K}} \left(1 + \sqrt{1 - \frac{2b\bar{K}\eta^2}{3\bar{G}}} \right) \right)^b} \quad (32)$$

where $\eta = \frac{q}{p}$, and $q = \sqrt{\frac{3}{2}\sigma'_{\alpha\beta}\sigma'_{\alpha\beta}}$ is the triaxial shear stress. Notably, both V_p^{hyper} and V_s^{hyper} can become imaginary when $\eta = \sqrt{\frac{3\bar{G}}{2b\bar{K}}}$, which indicates material instability [27, 36, 37]. Such instabilities have also been documented in other hyperelastic models by evaluating the convexity of the energy [10, 20]. Moreover, the transverse wave speed depends only on the stress invariants; thus, for triaxial states, the wave perturbation direction plays no role in the wave speed when the wave propagates along a principal direction as illustrated in fig. 3.

To understand the differences between the models, wave speed predictions are compared with wave measurements obtained from experimental data, which were digitised from results presented by [35]. The triaxial experiment conducted was a drained compression test on dry sand, ensuring that the wave speeds would not be influenced by the presence of water [38–40]. The experiments were performed under a radial stress $\sigma_r = 100$ kPa for three different initial solid fractions: $\phi_0 \approx 0.52$, $\phi_0 \approx 0.55$, and $\phi_0 \approx 0.60$. It is crucial to highlight that the densest experiment ($\phi_0 \approx 0.60$) experienced shear localisation [35]. Therefore, experimental results are shown only up to the peak stress ($\varepsilon^a \approx 0.04$) for this experiment, and specimen homogeneity cannot be assumed. There are no free parameters in the prediction at this stage since the stiffnesses obtained from the previous section in isotropic experiments are kept the same, which are shown in table II.

fig. 4 plots the transverse and longitudinal velocities against the axial strain. The hyperelastic model underpredicts the experimental data for the transverse wave velocities, whereas the hypoelastic model under or overpredicts experimental data depending on the initial density. However, the hyperelastic model generally offers a more accurate prediction to the data for longitudinal wave speed than the hypoelastic model. Notably, for $\phi_0 \approx 0.60$, the hyperelastic model could not produce a prediction beyond the red dotted line in fig. 4 (c) as these stress states resulted in an imaginary wave speed, suggesting the emergence of an instability. However, this occurred earlier than the peak stress of the experiment.

The observations are further substantiated by fig. 5, which compares the measured values with those predicted by both models. Encouragingly, both models predicted wave speeds are within a range of $\pm 10\%$ of the measured values, although the hyperelastic model tends to yield better results overall. Both models accurately reproduce shear wave velocities, although the hyperelastic model exceeds a -5% error for $\phi_0 \approx 0.52$. However, the hyperelastic model outperforms predicting longitudinal wave speeds and essentially stays within the $\pm 10\%$ error range

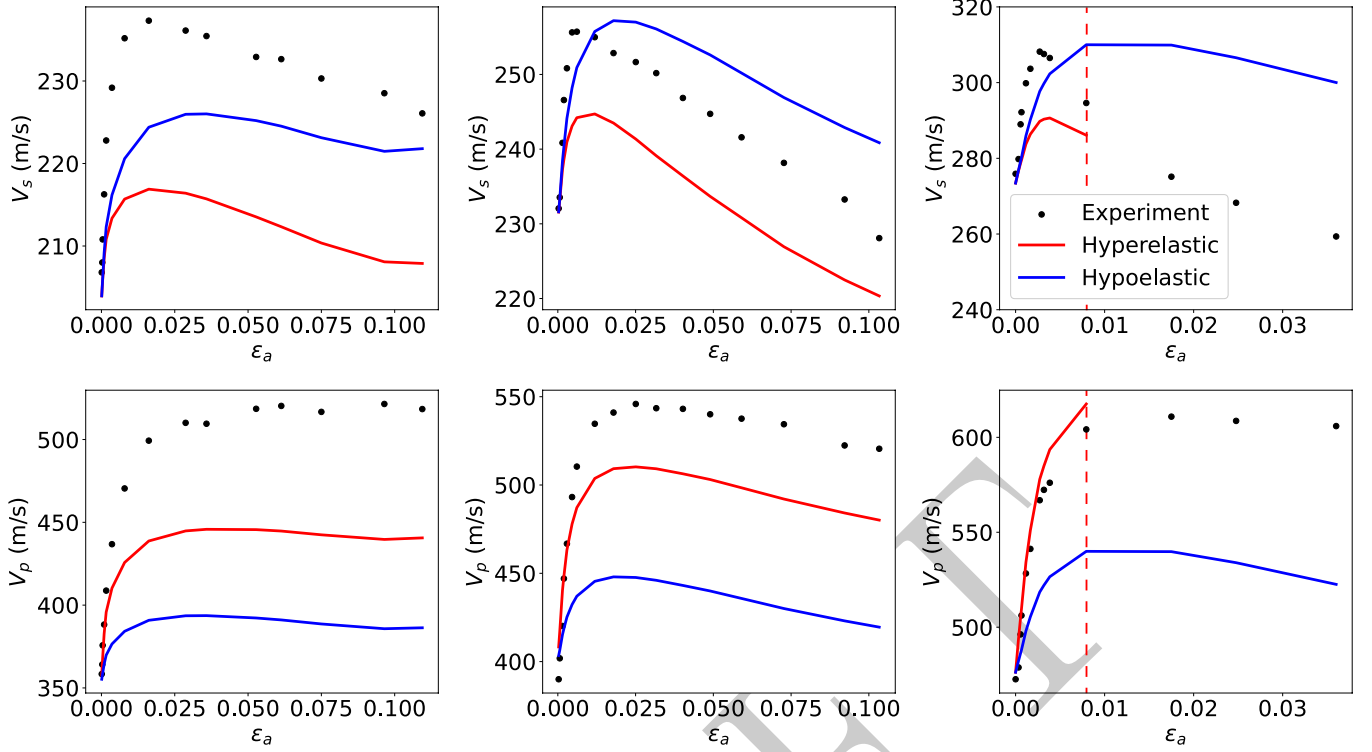


FIG. 4. Variation of V_s (top row) and V_p (bottom row) against axial strain ε^a for (a) $\phi_0 \approx 0.52$, (b) $\phi_0 \approx 0.55$, and (c) $\phi_0 \approx 0.60$. In (c), the red dashed line highlights the point beyond which the hyperelastic model predicts material instability. Additionally, the experimental results in (c) are limited to results up to the peak stress that occurred at $\varepsilon^a \approx 0.04$ as the experiment underwent a shear band, as stated in [35]. The experimental data was extracted from [35].

for $\phi_0 \approx 0.55$ and $\phi_0 \approx 0.60$. The hypoelastic model exceeds a -10% error in these cases. These results suggest that the additional stress-dependent terms in the hyperelastic model provide correction factors missing in the hypoelastic models.

C. Material isotropy

Lastly, the V_p/V_s ratio is examined to explore shearing-induced differences in the evolution of V_p and V_s . fig. 6 illustrates the variation of V_p/V_s against ε^a . Notably, the data reveals an initial increase of V_p/V_s before plateauing, with $\phi_0 \approx 0.60$ not exhibiting a plateau as the experimental results are not shown beyond $\varepsilon^a \approx 0.04$ (peak stress). However, the hypoelastic model maintains a constant ratio because the power law coefficients are assumed to be identical for both V_p and V_s as is required for isotropic materials. One might argue that the power coefficients should differ for empirical relations eqs. (3) and (4) or include fabric dependency [41, 42], leading to some evolution of V_p/V_s , and therefore, extending the empirical models to anisotropic materials. However, the hyperelastic model captures this evolution without additional assumptions (or extra parameters) thanks to the additional stress-dependent terms that arise when

deriving the wave speeds. The prediction of evolving V_p/V_s suggests that, at least to a first-order, incorporating a more sophisticated stress dependency or fabric might not be essential as discussed in Mayer and Liu [25]. This offers a compelling methodology to accurately account for stress-induced anisotropy and inherent material anisotropy, enhancing our understanding of prevailing mechanisms within soils.

IV. CONCLUSIONS

In this paper, wave speeds were derived for hyperelastic and hypoelastic models that depend on pressure and density in a general manner. The hypoelastic model's wave speed is equivalent to the empirical relations. The hyperelastic model is also equivalent to the empirical relations for isotropic compression.

However, for triaxial states, the wave speeds of the hyperelastic model become more elaborate, revealing previously unobserved stress dependencies, which are not present in the hypoelastic model. The hypoelastic model, equivalent to the empirical relations, generally mirrors the overall trends in longitudinal and transverse wave speed. Yet, it does not accurately capture the evolution of their ratios V_p/V_s . Conversely, the hyperelastic model

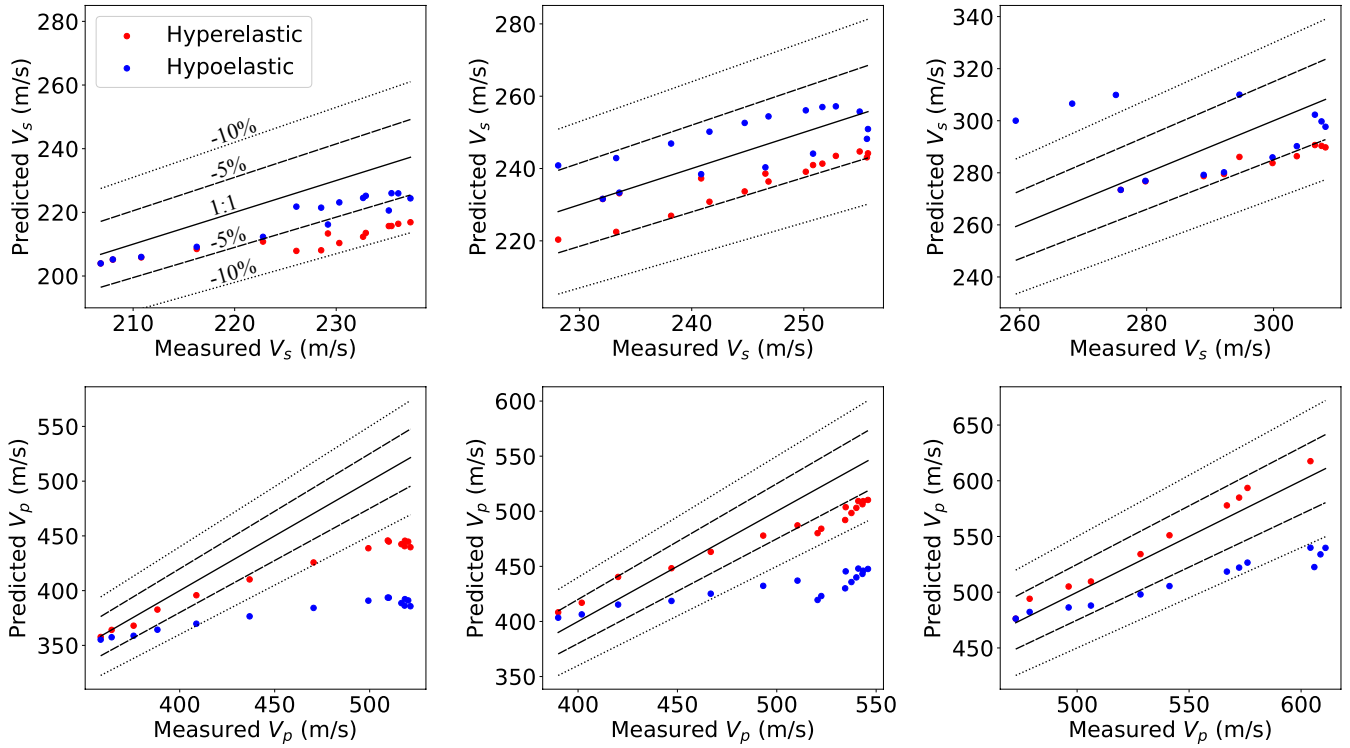


FIG. 5. Predicted V_s (top row) and V_p (bottom row) against experimentally measured velocities for (a) $\phi_0 \approx 0.52$, (b) $\phi_0 \approx 0.55$, and (c) $\phi_0 \approx 0.60$. The solid black line denotes the agreement line with a slope of 1, the dashed line represents $\pm 5\%$ error of a perfect prediction, and the dotted line is $\pm 10\%$ error.

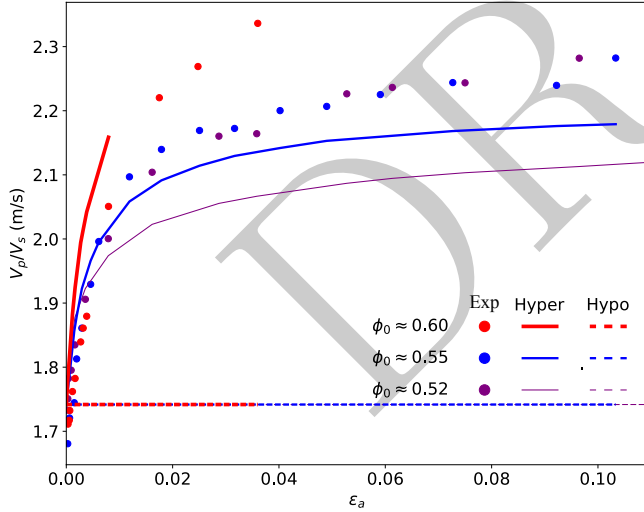


FIG. 6. Variation of V_p/V_s against axial strain ε^a . The results for the experiment (solid points), the hyperelastic model (solid line), and the hypoelastic model (dashed line) are plotted for $\phi \approx 0.60$ (red), $\phi \approx 0.55$ (blue).

predicts an evolution in the ratios of the longitudinal and transverse waves due to these additional stress dependencies arising from terms ensuring energy conservation. This suggests that material anisotropy may not be re-

quired for a first-order approximation of the evolution of V_p/V_s . Furthermore, these intricate stress dependencies might illuminate the observed evolution of V_p under high stresses in oedometric compression [43, 44]. More specifically, these findings emerge from not losing energy while waves travel in hyperelastic media, unlike the case of hypoelastic media, and from the consistently derived wave speeds for pressure-dependent elastic media.

Additionally, it is paramount to highlight that the analytical derivation allows the isolation of the true elastic constants of the material, in contrast to the aggregated parameters frequently assumed in empirical correlations. This distinction is pivotal, as elastic stiffness often serves as a benchmark for design methodologies [1, 3] and model calibration [45–47].

Finally, the derived transverse wave speed for hyperelasticity indicates that the wave propagation direction does not affect triaxial states when propagating along principal directions. This suggests that there is a necessity for either fabric or an anisotropic constitutive model to reproduce experimental results for materials that produce this effect [48–50]. Furthermore, this procedure could be extended to incorporate other state variables, such as fabric, grain size and shape, as well as saturation. Thus, it provides a methodological and consistent manner in which the effect of additional state variables on wave speed can be considered.

- [1] J. Atkinson, Non-linear soil stiffness in routine design, *Géotechnique* **50**, 487 (2000).
- [2] P. W. Mayne, Stress-strain-strength-flow parameters from enhanced in-situ tests, in *Proc. Int. Conf. on In Situ Measurement of Soil Properties and Case Histories, Bali* (2001) pp. 27–47.
- [3] C. Clayton, Stiffness at small strain: research and practice, *Géotechnique* **61**, 5 (2011).
- [4] B. O. Hardin and F. Richart Jr, Elastic wave velocities in granular soils, *Journal of the Soil Mechanics and Foundations Division* **89**, 33 (1963).
- [5] B. O. Hardin and G. E. Blandford, Elasticity of particulate materials, *Journal of Geotechnical Engineering* **115**, 788 (1989).
- [6] T. Wichtmann and T. Triantafyllidis, Influence of the grain-size distribution curve of quartz sand on the small strain shear modulus G_{max} , *Journal of geotechnical and geoenvironmental engineering* **135**, 1404 (2009).
- [7] Y. Li, M. Otsubo, and R. Kuwano, Evaluation of soil fabric using elastic waves during load-unload, *Journal of Rock Mechanics and Geotechnical Engineering* (2022).
- [8] C. Santamarina and G. Cascante, Effect of surface roughness on wave propagation parameters, *Geotechnique* **48**, 129 (1998).
- [9] S. Yimsiri and K. Soga, Micromechanics-based stress-strain behaviour of soils at small strains, *Géotechnique* **50**, 559 (2000).
- [10] I. Agnolin and J.-N. Roux, Internal states of model isotropic granular packings. iii. elastic properties, *Physical Review E* **76**, 061304 (2007).
- [11] J. D. Goddard, Nonlinear elasticity and pressure-dependent wave speeds in granular media, *Proceedings of the royal society of London. Series A: mathematical and physical sciences* **430**, 105 (1990).
- [12] S. K. Roesler, Anisotropic shear modulus due to stress anisotropy, *Journal of the Geotechnical Engineering Division* **105**, 871 (1979).
- [13] P. Yu and F. Richart Jr, Stress ratio effects on shear modulus of dry sands, *Journal of Geotechnical Engineering* **110**, 331 (1984).
- [14] R. Bellotti, M. Jamiołkowski, D. L. Presti, and D. O’neill, Anisotropy of small strain stiffness in ticino sand, *Géotechnique* **46**, 115 (1996).
- [15] T. Wichtmann and T. Triantafyllidis, On the influence of the grain size distribution curve on p-wave velocity, constrained elastic modulus m_{max} and poisson’s ratio of quartz sands, *Soil Dynamics and Earthquake Engineering* **30**, 757 (2010).
- [16] M. Payan, K. Senetakis, A. Khoshghalb, and N. Khalili, Effect of gradation and particle shape on small-strain young’s modulus and poisson’s ratio of sands, *International Journal of Geomechanics* **17**, 04016120 (2017).
- [17] X. Liu and J. Yang, Shear wave velocity in sand: effect of grain shape, *Géotechnique* **68**, 742 (2018).
- [18] X. Tang and J. Yang, Wave propagation in granular material: What is the role of particle shape?, *Journal of the Mechanics and Physics of Solids* **157**, 104605 (2021).
- [19] U. Mital, R. Kawamoto, and J. E. Andrade, Effect of fabric on shear wave velocity in granular soils, *Acta Geotechnica* **15**, 1189 (2020).
- [20] Y. Jiang and M. Liu, Granular elasticity without the coulomb condition, *Physical Review Letters* **91**, 144301 (2003).
- [21] I. Einav and A. M. Puzrin, Pressure-dependent elasticity and energy conservation in elastoplastic models for soils, *Journal of Geotechnical and Geoenvironmental engineering* **130**, 81 (2004).
- [22] G. Houslyby, A. Amorosi, and E. Rojas, Elastic moduli of soils dependent on pressure: a hyperelastic formulation, *Géotechnique* **55**, 383 (2005).
- [23] G. D. Nguyen and I. Einav, The energetics of cataclasis based on breakage mechanics, *Pure and applied geophysics* **166**, 1693 (2009).
- [24] B. Andreotti, Y. Forterre, and O. Pouliquen, *Granular media: between fluid and solid* (Cambridge University Press, 2013).
- [25] M. Mayer and M. Liu, Propagation of elastic waves in granular solid hydrodynamics, *Physical Review E* **82**, 042301 (2010).
- [26] I. Stefanou and S. Alevizos, Fundamentals of bifurcation theory and stability analysis, *Instabilities Modeling in Geomechanics*, 31 (2016).
- [27] I. Stefanou and E. Gerolymatou, Strain localization in geomaterials and regularization: rate-dependency, higher order continuum theories and multi-physics, *ALERT Doctoral School* **780**, 47 (2019).
- [28] E. Alaei, B. Marks, and I. Einav, A hydrodynamic-plastic formulation for modelling sand using a minimal set of parameters, *Journal of the Mechanics and Physics of Solids* **151**, 104388 (2021).
- [29] M. B. Rubin and I. Einav, A large deformation breakage model of granular materials including porosity and inelastic distortional deformation rate, *International Journal of Engineering Science* **49**, 1151 (2011).
- [30] D. Riley, I. Einav, and F. Guillard, A constitutive model for porous media with recurring stress drops: From snow to foams and cereals, *International Journal of Solids and Structures* **262**, 112044 (2023).
- [31] Y. Chen, F. Guillard, and I. Einav, A hydrodynamic model for chemo-mechanics of poroelastic materials, *Géotechnique*, 1 (2023).
- [32] L. D. Landau, E. M. Lifshitz, A. M. Kosevich, and L. P. Pitaevskii, *Theory of elasticity: volume 7*, Vol. 7 (Elsevier, 1986).
- [33] J. Achenbach, *Wave propagation in elastic solids* (Elsevier, 2012).
- [34] M. Zytynski, M. Randolph, R. Nova, and C. Wroth, On modelling the unloading-reloading behaviour of soils, *International Journal for Numerical and Analytical Methods in Geomechanics* **2**, 87 (1978).
- [35] T. Dutta, M. Otsubo, and R. Kuwano, Effect of shearing history on stress wave velocities of sands observed in triaxial compression tests, *Soils and Foundations* **61**, 541 (2021).
- [36] J. Rice, The localization of plastic deformation, in *Theoretical and Applied Mechanics. 14th IUTAM Congress*, edited by W. Koiter (North-Holland, Amsterdam, 1976) pp. 207–220.
- [37] Q. Zhang, Y. Li, M. Hou, Y. Jiang, and M. Liu, Elastic waves in the presence of a granular shear band formed by direct shear, *Physical Review E* **85**, 031306 (2012).
- [38] G. C. Cho and J. C. Santamarina, Unsaturated particu-

- late materials—particle-level studies, *Journal of geotechnical and geoenvironmental engineering* **127**, 84 (2001).
- [39] J. Barrière, C. Bordes, D. Brito, P. Sénéchal, and H. Perroud, Laboratory monitoring of p waves in partially saturated sand, *Geophysical Journal International* **191**, 1152 (2012).
- [40] E. Leong and Z. Cheng, Effects of confining pressure and degree of saturation on wave velocities of soils, *International Journal of Geomechanics* **16**, D4016013 (2016).
- [41] T. Dutta, M. Otsubo, R. Kuwano, and C. O’Sullivan, Evolution of shear wave velocity during triaxial compression, *Soils and Foundations* **60**, 1357 (2020).
- [42] Y. Li, M. Otsubo, and R. Kuwano, Dem analysis on the stress wave response of spherical particle assemblies under triaxial compression, *Computers and Geotechnics* **133**, 104043 (2021).
- [43] X. Jia, C. Caroli, and B. Velicky, Ultrasound propagation in externally stressed granular media, *Physical Review Letters* **82**, 1863 (1999).
- [44] H. A. Makse, N. Gland, D. L. Johnson, and L. Schwartz, Granular packings: Nonlinear elasticity, sound propagation, and collective relaxation dynamics, *Physical Review E* **70**, 061302 (2004).
- [45] M. Fahey and J. P. Carter, A finite element study of the pressuremeter test in sand using a nonlinear elastic plastic model, *Canadian Geotechnical Journal* **30**, 348 (1993).
- [46] F. Ayala, E. Sáez, and C. Magna-Verdugo, Computational modelling of dynamic soil-structure interaction in shear wall buildings with basements in medium stiffness sandy soils using a subdomain spectral element approach calibrated by micro-vibrations, *Engineering Structures* **252**, 113668 (2022).
- [47] Y. Huang, P. Wang, Y. Lai, and Z. Xu, A small-strain soil constitutive model for initial stiffness evaluation of laterally loaded piles in drained marine sand, *Ocean Engineering* **268**, 113417 (2023).
- [48] R. Kuwano and R. Jardine, On the applicability of cross-anisotropic elasticity to granular materials at very small strains, *Géotechnique* **52**, 727 (2002).
- [49] M. Zamanian, V. Mollaei-Alamouti, and M. Payan, Directional strength and stiffness characteristics of inherently anisotropic sand: The influence of deposition inclination, *Soil Dynamics and Earthquake Engineering* **137**, 106304 (2020).
- [50] J. Liu, M. Otsubo, Y. Kawaguchi, and R. Kuwano, Anisotropy in small-strain shear modulus of granular materials: Effects of particle properties and experimental conditions, *Soils and Foundations* **62**, 101105 (2022).